

Modulating electron density of vacancy site by single Au atom for effective CO₂ photoreduction

Yuehan Cao ^{1,2,7}, Lan Guo^{2,7}, Meng Dan^{2,3}, Dmitry E. Doronkin⁴, Chunqiu Han², Zhiqiang Rao², Yang Liu^{2,3}, Jie Meng^{3,5}, Zeai Huang², Kaibo Zheng^{3,5}, Peng Chen^{2,6}, Fan Dong ⁶ & Ying Zhou ^{1,2}✉

The surface electron density significantly affects the photocatalytic efficiency, especially the photocatalytic CO₂ reduction reaction, which involves multi-electron participation in the conversion process. Herein, we propose a conceptually different mechanism for surface electron density modulation based on the model of Au anchored CdS. We firstly manipulate the direction of electron transfer by regulating the vacancy types of CdS. When electrons accumulate on vacancies instead of single Au atoms, the adsorption types of CO₂ change from physical adsorption to chemical adsorption. More importantly, the surface electron density is manipulated by controlling the size of Au nanostructures. When Au nanoclusters downsize to single Au atoms, the strong hybridization of Au 5*d* and S 2*p* orbits accelerates the photo-electrons transfer onto the surface, resulting in more electrons available for CO₂ reduction. As a result, the product generation rate of Au_{5A}/Cd_{1-x}S manifests a remarkable at least 113-fold enhancement compared with pristine Cd_{1-x}S.

¹State Key Laboratory of Oil and Gas Reservoir Geology and Exploitation, Southwest Petroleum University, Chengdu, China. ²The Center of New Energy Materials and Technology, School of New Energy and Materials, Southwest Petroleum University, Chengdu, China. ³The Division of Chemical Physics and Nano-Lund, Lund University, Lund, Sweden. ⁴Institute for Chemical Technology and Polymer Chemistry and Institute of Catalysis Research and Technology, Karlsruhe Institute of Technology, Karlsruhe, Germany. ⁵Department of Chemistry, Technical University of Denmark, Kongens Lyngby, Denmark. ⁶Research Center for Environmental Science and Technology, Institute of Fundamental and Frontier Sciences, University of Electronic Science and Technology of China, Chengdu, China. ⁷These authors contributed equally: Yuehan Cao, Lan Guo. ✉email: yzhou@swpu.edu.cn

As a representative greenhouse gas, carbon dioxide (CO₂) has brought out serious environmental problems needing to solve urgently^{1,2}. Photocatalytic CO₂ conversion technology has attracted extensive interest, since the conversion of CO₂ into high value-added chemicals could potentially be achieved under relatively mild conditions, which facilitates its resource utilization^{3,4}. Generally, photocatalytic CO₂ conversion is a typical photoreduction reaction, which needs electrons to participate in^{5–7}. Different from other photoreduction reactions, such as hydrogen evolution reaction (two electrons), photocatalytic CO₂ conversion is an inherently multi-electron reduction process^{8–10}. To this end, photocatalysts are required to offer abundant electrons for the CO₂ molecule to promote its transformation in the reaction process¹¹.

Previous studies suggest that metals, especially noble metals, have been commonly introduced to enhance the surface electron density of photocatalysts^{12,13}. It is generally agreed that the photocatalytic performance is greatly dependent on the metal center and its local coordination. Since the local electron density will be redistributed after introducing metal and the majority of electrons are accumulated around the metal and its surrounding atoms^{14,15}, many efforts have focused on changing the metal center and/or ligands to achieve high efficiency for CO₂ photoreduction. With in-depth research, it is further found that electron transfer is tremendously dependent on the size of metal nanostructures or the type of local coordination^{16,17}. For instance, Wu et al. reported that the electrons have transferred from single Pt atoms to sulfur-doped carbon support and the direction of electron transfer will be reversed after loading Pt nanoclusters¹⁶. Meanwhile, Dai et al. found that the types of vacancies (boron or nitrogen vacancies) could affect the electron transfer direction between Pt nanoparticles and BN nanosheets¹⁷. Hence, it is speculated that the electrons may be localized at other sites instead of metal nanostructures. Indeed, previous studies suggest that the interaction of adsorbed CO₂ molecule and metal site is relatively weak since the formed metal–C or metal–O bonds are weaker than the highly stable C–O bonds in CO₂ molecule^{8,18,19}. This will lead to the easy cleaving of metal–C or metal–O bonds during the reaction process, hindering the further transformation of CO₂⁸. The above considerations suggest that controlling the size of metal nanostructures and/or the type of vacancies might realize the accumulation of electrons at other sites instead of metal nanostructures, which is likely to promote the adsorption and conversion of CO₂.

For this purpose, CdS is selected to be a model material due to the easy-fabricated vacancies and favorable solar light response^{20–22}. According to the pre-experiments in Supplementary Fig. 1, Au is chosen as the dopant metal^{23–25}. We have designed and fabricated a series of Au-anchored CdS photocatalysts and reported a conceptually different mechanism for modulating surface electron density to promote the conversion of CO₂. As displayed in Fig. 1, when the type of vacancies changes from S vacancies to Cd vacancies, the direction of electron transfer will be reversed after anchoring single Au atoms, resulting in the accumulation of electrons in neighboring Cd vacancies instead of single Au atoms. Benefiting from this, CO₂ could be chemically bonded on the Cd vacancies instead of physical adsorption on single Au atoms to promote its effective activation.

Results

Catalyst characterization. Based on the above considerations, the CdS with Cd vacancies (Cd_{1–x}S) is first prepared by the hydrothermal method. X-ray diffraction (XRD) pattern and transmission electron microscopy (TEM) images (cf. Fig. 2a and Supplementary Fig. 2a, b) of the synthesized sample display that

hexagonal CdS with the nanoparticle morphology is fabricated. Meanwhile, the electron paramagnetic resonance (EPR) signals with the *g* factor of 1.99 and 2.03 are observed for the synthesized sample (cf. Supplementary Fig. 3), which are ascribed to sulfur atoms surrounding Cd vacancies in hexagonal CdS^{26–28}. According to the element analysis, the ratios of Cd and S are quantitated as 0.76:1 (cf. Supplementary Table 1). The above results confirm the existence of Cd vacancies in the synthesized sample. After Au loading, XRD patterns of both 1%Au/Cd_{1–x}S and 2%Au/Cd_{1–x}S samples have rarely changed compared with Cd_{1–x}S (cf. Fig. 2a). For 1%Au/Cd_{1–x}S, there are no Au nanostructures observed in TEM and HRTEM images (cf. Supplementary Fig. 2c, d). Hence, to reveal the atomic-resolution structure of 1%Au/Cd_{1–x}S sample, aberration-corrected high-angle annular dark-field scanning TEM is shown in Fig. 2b. The bright spots corresponding to heavy Au atoms (marked by yellow circles) are homogeneously dispersed, indicating that the Au atoms are atomically dispersed on the Cd_{1–x}S. Meanwhile, the element mapping of the 1%Au/Cd_{1–x}S (cf. Fig. 2c) shows the uniform distribution of Au, Cd, and S elements. With the increase of loading content, some nanoparticles are observed in TEM and HRTEM images of 2%Au/Cd_{1–x}S sample (cf. Supplementary Fig. 2e, f). The interplanar distance in these nanoclusters is ca 1.15 Å corresponding to the (222) planes of metallic Au²⁹. This is indicated that part of single Au atoms is aggregated together to form the Au nanoclusters with the increase of loading content. According to the size distributions of Au nanoclusters and element mapping in Supplementary Fig. 4, the Au nanoclusters are homogeneously distributed on Cd_{1–x}S and the sizes of Au nanoclusters are mainly in the range of 1–3 nm. The above results indicate that the single Au atoms (Au_{SA}) and Au clusters (Au_{NC}) are successfully introduced in the 1%Au/Cd_{1–x}S and 2%Au/Cd_{1–x}S samples, respectively. To distinguish Au nanostructures in different samples, 1%Au/Cd_{1–x}S and 2%Au/Cd_{1–x}S samples are referred as Au_{SA}/Cd_{1–x}S and Au_{NC}/Cd_{1–x}S for simplicity in the following study.

To investigate the coordination environments of Au in the Au_{SA}/Cd_{1–x}S sample, Au L₃-edge X-ray absorption near-edge structure (XANES) and extended X-ray absorption fine structure (EXAFS) spectra are presented in Fig. 2d, e. The white line peak of Au_{SA}/Cd_{1–x}S sample is different from that of the reference Au foil. The EXAFS spectrum shows that Au_{SA}/Cd_{1–x}S exhibits a peak near 1.7 Å without any significant Au–Au contribution between 2 and 4 Å, confirming the atomic dispersion of Au on Cd_{1–x}S. The quantitative structural parameters of Au in the Au_{SA}/Cd_{1–x}S (cf. Supplementary Table 2) demonstrate that one Au atom is bonded with two or three S atoms to form the Au–S bonds. To further identify the loading position of single Au atoms, EPR spectra are carried out in Supplementary Fig. 5. The intensities of EPR signals assigned to Cd vacancies decreased after introducing single Au atoms, indicating that part of Cd vacancies are covered by single Au atoms. Furthermore, the models of Au-loaded Cd_{1–x}S surface with different sites (surface S and Cd vacancy) are constructed by density functional theory (DFT) method (cf. Supplementary Table 3). The calculated formation energy of single Au atom anchored on Cd vacancy is –5.30 eV, which is much more negative than that on surface S atoms (*E_f* = –1.89 eV). It is hence suggested that single Au atoms are anchored on the Cd vacancies to form the Au–S bonds in the Au_{SA}/Cd_{1–x}S sample.

Similarly, the CdS with S vacancies (CdS_{1–x}) is synthesized by the hydrothermal method (cf. Supplementary Fig. 6). There are no EPR signals assigned to S vacancies observation in the synthesized sample (cf. Supplementary Fig. 7). To confirm the existence of S vacancies, the Cd K-edge XANES and EXAFS spectra of CdS_{1–x} and pristine CdS (CdS) samples are shown in

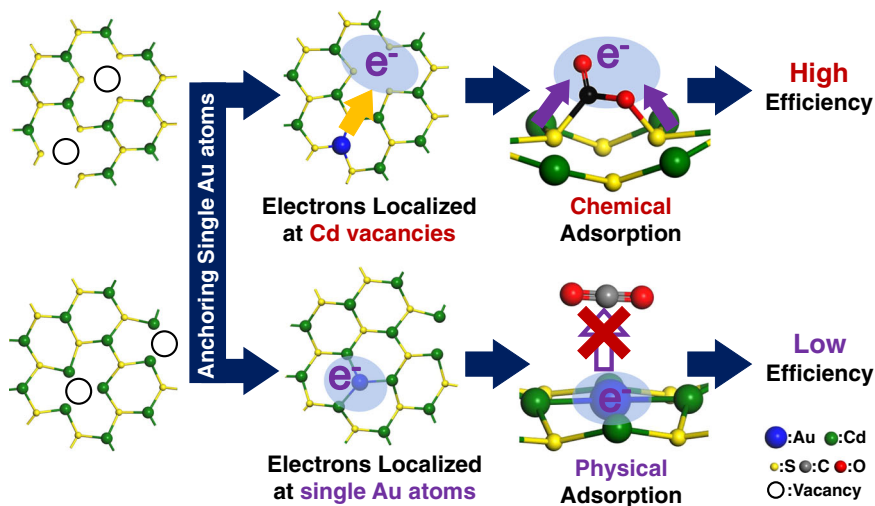


Fig. 1 Photocatalytic mechanism. Schematic illustration of single Au atoms in CdS to promote CO₂ photoreduction.

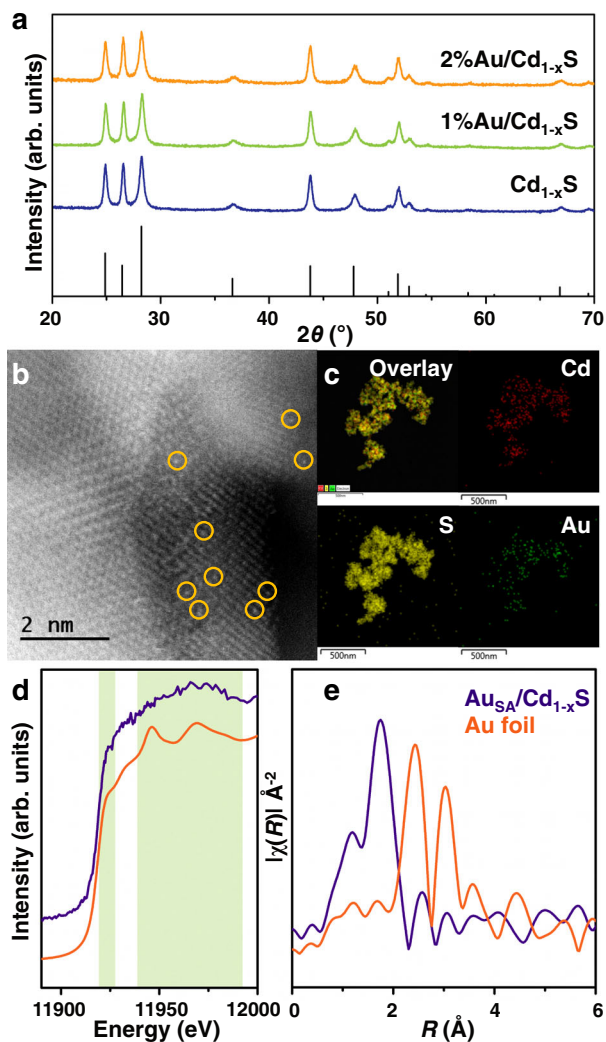


Fig. 2 Characterizations. **a** XRD patterns of Cd_{1-x}S, 1%Au/Cd_{1-x}S, and 2%Au/Cd_{1-x}S samples. **b** HAADF-STEM image of 1%Au/Cd_{1-x}S, single atomic Au sites high-lighted by yellow circles. **c** Elemental mappings of 1%Au/Cd_{1-x}S. **d** XAFS analysis of Au_{SA}/Cd_{1-x}S: Au L₃ XANES spectra of the sample and the reference foil. **e** Corresponding k¹-weighted Fourier transform (FT) EXAFS spectra.

Supplementary Fig. 8. The white line peak of the CdS_{1-x} is similar to that of the CdS and both of them are different from that of the reference Cd foil. According to the EXAFS spectra, the CdS sample shows bulk crystalline CdS. In the case of the CdS_{1-x} sample, intensity of the first coordination shell is lower than that of CdS, implying fewer S-neighbors than in the bulk CdS. Combined with the element analysis, the ratio of Cd and S are quantitated as 1:0.73 (cf. Supplementary Table 1). It is confirmed that there are S vacancies in the CdS_{1-x} sample.

Furthermore, the same impregnation method is employed to synthesize the 1%Au/CdS_{1-x} and 2%Au/CdS_{1-x} (cf. Supplementary Fig. 6). The XANES and EXAFS spectra of CdS_{1-x} and 1%Au/CdS_{1-x} are shown in Supplementary Fig. 9 and 10. It is found that the intensity of the first coordination shell in CdS_{1-x} sample increases after loading Au, suggesting that part of S vacancies are filled with Au (cf. Supplementary Fig. 9). Meanwhile, in the case of 1%Au/CdS_{1-x}, there are no significant peaks assigned to Au–Au bonds found in the range of 2–4 Å, confirming the atomic dispersion of Au on CdS_{1-x} (cf. Supplementary Fig. 10). The above results suggest that single Au atoms are anchored on the S vacancies. Hence, the 1%Au/CdS_{1-x} sample is referred to Au_{SA}/CdS_{1-x}.

In brief, the CdS samples with different types of vacancies (Cd and S vacancies) are successfully fabricated and the introduced single Au atoms are anchored on the vacancies. In the case of the Au-anchored Cd_{1-x}S systems, with the increase of loading content, Au has changed from single atoms into nanoclusters.

Photocatalytic CO₂RR measurement. As depicted in Fig. 3 and Supplementary Fig. 11, photocatalytic CO₂ reduction tests are carried out to evaluate the effect of Au on photoreduction efficiency. Cd_{1-x}S shows low CO and CH₄ generation rates of 0.2 and 0.1 μmol g⁻¹ h⁻¹, respectively. After anchoring Au nanoclusters, the product generation rates are enhanced. It is interesting that with the introduction of single Au atoms, the CO, CH₄, and H₂ generation rates are highly promoted to 32.2, 11.3, and 7.9 μmol g⁻¹ h⁻¹, respectively. It manifests a remarkable 161-fold and 113-fold enhancement over Cd_{1-x}S as well as 5-fold, 4-fold, and 2-fold enhancement compared with Au_{NC}/Cd_{1-x}S. For CdS_{1-x} systems (cf. Fig. 3b), the introduction of Au brings out an enhancement of CO₂ photoreduction efficiency as well. Among all the samples, Au_{SA}/CdS_{1-x} reveals the highest CO₂ photoreduction efficiency with the CO, CH₄, and H₂ generation rates of 3.7, 0.4, and 0.2 μmol g⁻¹ h⁻¹, which is a 2-fold, 4-fold, and 2-fold enhancement compared over the pristine CdS_{1-x}. The

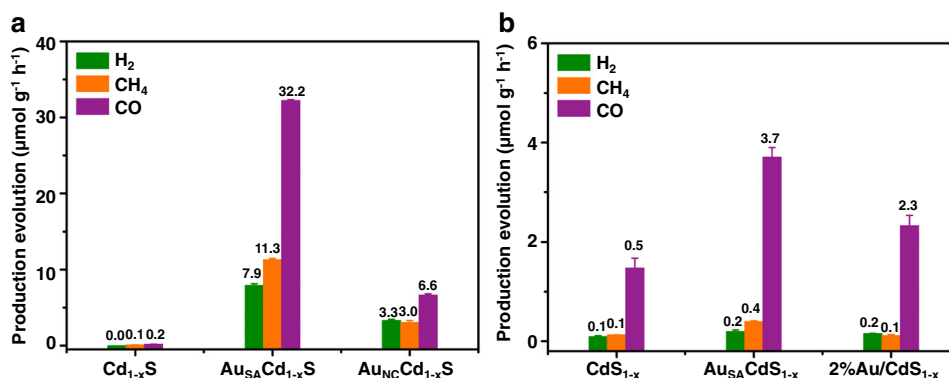


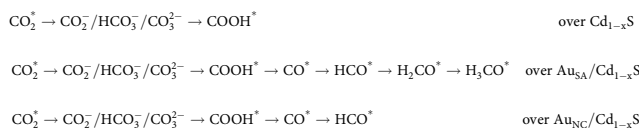
Fig. 3 The photocatalytic performance of CO₂RR. Average yield in the photocatalytic conversion of CO₂ with H₂O in the presence of water vapor under UV-visible light. **a** Over Cd_{1-x}S, Au_{SA}/Cd_{1-x}S, and Au_{NC}/Cd_{1-x}S samples. **b** Over CdS_{1-x}, Au_{SA}/CdS_{1-x}, and 2%Au/CdS_{1-x} samples. The error bar was drawn based on the calculated standard error of two parallel tests.

above results indicate that, compared with S vacancies, single Au atoms bring much more significant improvement for CO₂ photoreduction efficiency when they are anchored on Cd vacancies. Meanwhile, when Au changes from single atoms into nanoclusters, the CO₂ photoreduction efficiency is gradually decreased. Furthermore, the photocatalytic CO₂RR performance of Au_{SA}/Cd_{1-x}S is relatively satisfactory compared with that of other metal sulfide, CdS-based, and noble-metal based photocatalysts in the published works (cf. Supplementary Table 4)^{8,30–38}. To confirm that the CO and CH₄ products are generated from the CO₂ conversion driven by Au_{SA}/Cd_{1-x}S, the isotope labeling is conducted using ¹³CO₂ as the reactant for qualitative analysis. Supplementary Fig. 12 displays that the generated CO and CH₄ originate from the CO₂ conversion driven by Au_{SA}/Cd_{1-x}S sample instead of desorption of adsorbed species from the surface. Besides, the peak at *m/z* = 32 is detected, which is assigned to generated oxidation product O₂. With a comparison of XRD, TEM, and HRTEM images between fresh and used Au_{SA}/Cd_{1-x}S samples (cf. Supplementary Fig. 13 and 14), the single Au atoms is not aggregated during the reaction process, indicating good stability.

Discussion

CO₂ adsorption during photocatalysis. To uncover the main factors of enhanced photocatalytic CO₂ reduction performance, solar light absorption is first investigated by UV-vis spectroscopy (cf. Supplementary Fig. 15). The absorption edges of Au_{SA}/Cd_{1-x}S and Au_{NC}/Cd_{1-x}S have barely changed compared with Cd_{1-x}S. For the CdS_{1-x} system, the introduction of Au does not change the absorption edge as well. This suggests that solar light absorption is not the determining factor in the photocatalytic CO₂ reduction performance. After light illumination, the excited electrons will finally transfer to the surface of the catalyst and combine with the adsorbed species to promote their conversion. The conversion of CO₂ involves the following steps. The adsorption of CO₂ on the surface of photocatalyst is the prerequisite step, which is relatively difficult due to the closed-shell electronic configuration of CO₂. Then, adsorbed CO₂ will obtain electrons from the surface to generate the carbon active species (e.g., CO₂⁻, HCO₃⁻, CO₃²⁻). These first two steps are aimed to activate the C–O bond of CO₂ molecule. Finally, these species will be further transformed into the desired products (e.g., CO, CH₄), which need abundant electrons to take part in to promote their effective transformation. Hence, the adsorption behavior of CO₂ not only determines the occurrences of reaction, but significantly affects the conversion efficiency.

Based on these considerations, in situ diffuse reflectance infrared Fourier transform spectroscopy (DRIFTS) is performed to detect the generated intermediates during the CO₂ adsorption process on the surfaces of Cd_{1-x}S and CdS_{1-x} systems (cf. Fig. 4 and Supplementary Fig. 16). For pristine Cd_{1-x}S (cf. Fig. 4a), there are some absorption bands assigned to bicarbonate (HCO₃⁻; δ(COH): 1200 and 1166 cm⁻¹), monodentate carbonate (m-CO₃²⁻; ν(C–O): 1140–1030 cm⁻¹) and carboxylate (CO₂⁻; ν(O–C–O)_s: 1266 cm⁻¹) detected with the prolonged time of adsorption³⁹. Meanwhile, the band assigned to COOH* is detected at 1634 cm⁻¹,^{40,41} suggesting that the adsorbed CO₂ is combined with H* and partly converted to the COOH*. After anchoring Au clusters, the intensities of absorption bands assigned to HCO₃⁻, CO₂⁻, and COOH* have decreased. There is a new band appearing at 1043 cm⁻¹, which is assigned to HCO*^{42,43}. This indicates that part of the formed COOH* is converted to HCO*. Different from it, some of the absorption bands (HCO₃⁻ and COOH*) almost disappear over Au_{SA}/Cd_{1-x}S. It should be noted that there is a new band detected at 1110 cm⁻¹ assigned to H₃CO*^{44,45}. The intensity of the absorption bands assigned to HCO* is much lower than that over Au_{NC}/Cd_{1-x}S, revealing that the majority of formed COOH* are quickly converted into HCO* and then transform into H₃CO*. The conversion pathway of CO₂ over different samples in Au/Cd_{1-x}S systems during the adsorption process could be deduced as follows:



It is indicated that the introduction of Au significantly promotes the further conversion of CO₂ on Cd_{1-x}S surface. When Au nanoclusters downsize to single Au atoms, the carbon active species can be deeply converted into H₃CO*, which is beneficial for the subsequent reaction. Different from the Cd_{1-x}S system, with the introduction of Au nanostructures, there are no absorption bands assigned to new intermediates appearing on CdS_{1-x} surface in the process of CO₂ adsorption (cf. Supplementary Fig. 16). It could be concluded that the introduction of Au has a slight effect in the CO₂ adsorption and conversion on CdS_{1-x} surface.

The above discussions suggest that the types of vacancies and the size of Au nanostructures present a different effect on the intermediates in the CO₂ adsorption process. In previous studies, reaction sites have possibly affected the generation of intermediates⁴⁶. Based on it, Au nanostructures (Au site) and

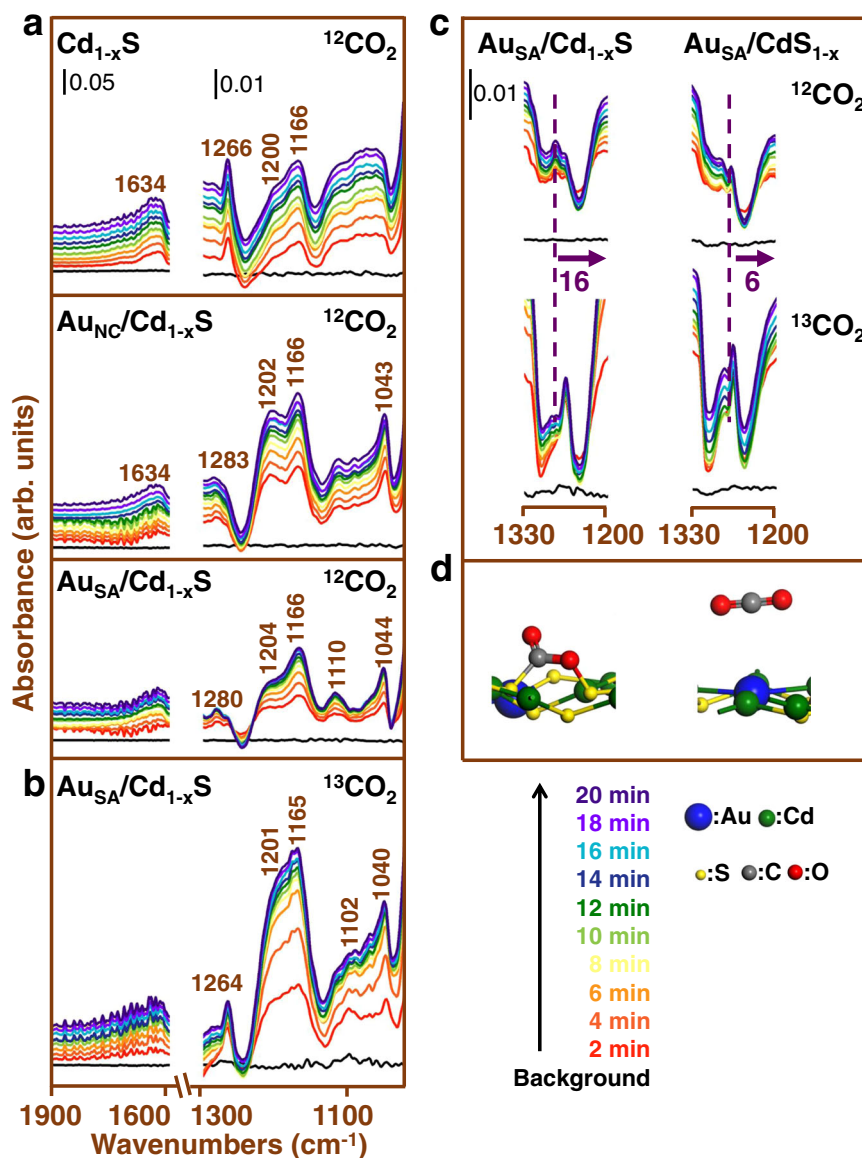


Fig. 4 In situ DRIFTS measurement. **a** In situ DRIFTS spectra of the $^{12}\text{CO}_2$ adsorption process over Cd_{1-x}S , $\text{Au}_{\text{NC}}/\text{Cd}_{1-x}\text{S}$, and $\text{Au}_{\text{SA}}/\text{Cd}_{1-x}\text{S}$. **b** In situ DRIFTS spectra of the $^{13}\text{CO}_2$ adsorption process over $\text{Au}_{\text{SA}}/\text{Cd}_{1-x}\text{S}$. **c** The comparison between in situ DRIFTS spectra of $^{12}\text{CO}_2$ and $^{13}\text{CO}_2$ adsorption process over $\text{Au}_{\text{SA}}/\text{Cd}_{1-x}\text{S}$ and $\text{Au}_{\text{SA}}/\text{CdS}_{1-x}$. **d** The adsorption models of CO_2 on different surfaces on single Au atom in $\text{Au}_{\text{SA}}/\text{CdS}_{1-x}$ and on Cd vacancy in $\text{Au}_{\text{SA}}/\text{Cd}_{1-x}\text{S}$.

vacancies (vacancy site) are selected to be the different CO_2 adsorption sites. The CO_2 adsorption models on $\text{Au}/\text{Cd}_{1-x}\text{S}$ and $\text{Au}/\text{CdS}_{1-x}$ are constructed by the DFT method (cf. Fig. 5 and Supplementary Fig. 17 and 18). The corresponding adsorption energies are summarized in Supplementary Table 5. For the pristine CdS_{1-x} , CO_2 will spontaneously adsorb on the S vacancies due to the negative adsorption energy. After anchoring single Au atoms, the adsorption energies change slightly compared with that of pristine CdS_{1-x} . According to the comparison of adsorption energies, CO_2 prefers to adsorb on single Au atoms instead of S vacancies. Similarly, in the case of pristine Cd_{1-x}S , CO_2 will also spontaneously adsorb on the Cd vacancies ($E_{\text{ads}} = -0.43$ eV). With the introduction of single Au atoms, the adsorption energy has significantly decreased, implying that single Au atoms promotes the adsorption of CO_2 on Cd_{1-x}S surface. It should be noted that CO_2 is more likely to adsorb on the Cd vacancies instead of single Au atoms due to the more negative adsorption energy. To further identify the adsorption site in $\text{Au}_{\text{SA}}/\text{Cd}_{1-x}\text{S}$, the different surfaces are probed

by N_2 sorption (cf. Supplementary Fig. 19). The specific surface area of Cd_{1-x}S (25.4 m^2/g) has increased after anchoring single Au atoms (33.9 m^2/g). It is suggested that the introduction of single Au atoms enhances the amount of adsorption site. However, the CO_2 adsorption capacity of Cd_{1-x}S is decreased from 72.9 to 66.2 $\mu\text{mol g}^{-1}$ (cf. Supplementary Fig. 20) after introducing single Au atoms. It is hence confirmed that the real adsorption sites of CO_2 in $\text{Au}_{\text{SA}}/\text{Cd}_{1-x}\text{S}$ should be the vacancies instead of single Au atoms. Furthermore, combined with in situ DRIFTS spectra, CO is used as the probe to identify the reactive reaction site of CO_2 reduction on $\text{Au}_{\text{SA}}/\text{Cd}_{1-x}\text{S}$ surface (cf. Supplementary Fig. 21). The absorption bands at 2170 and 2109 cm^{-1} are assigned to gaseous CO ⁴⁷. Furthermore, the absorption band assigned to C=O bond and S-O are detected on the surface ($\nu(\text{C}=\text{O})$: 1621 cm^{-1} ; $\nu(\text{S}-\text{O})$: 1209 and 1162 cm^{-1})⁴⁷⁻⁵¹. It is suggested that the CO molecule adsorbs on the Cd vacancy sites and combines with the S atoms to form C=O-S bonds. Meanwhile, there are some absorption bands detected at 1100 and 1044 cm^{-1} , which are assigned to HCO^* and H_3CO^* . The

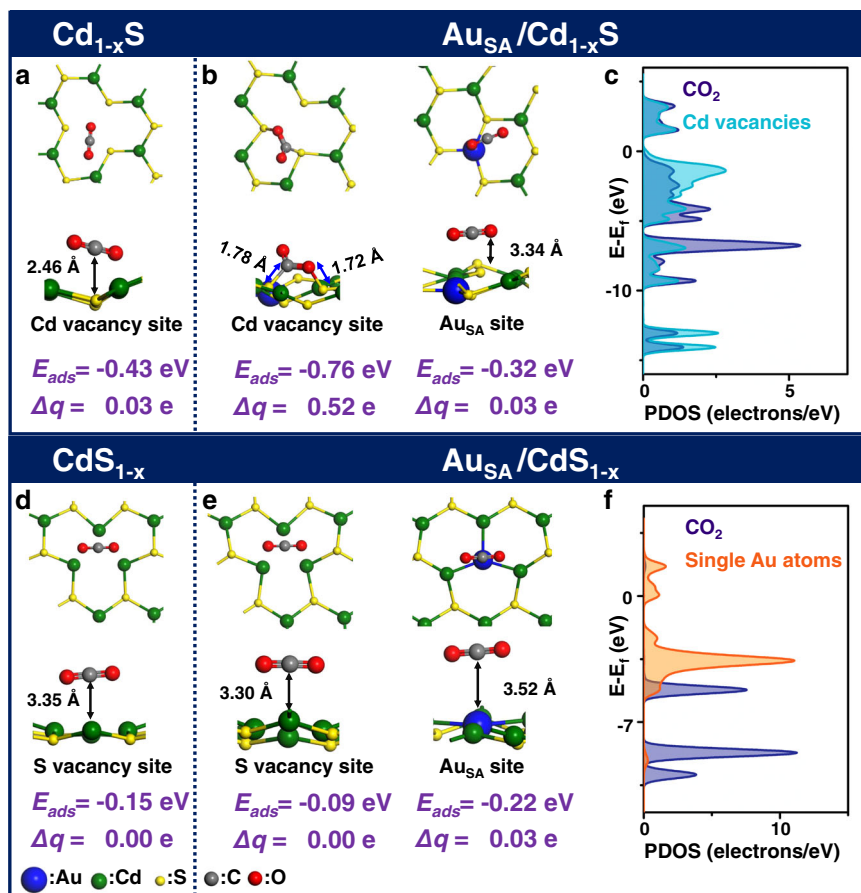


Fig. 5 CO₂ adsorption models on different surfaces. Configurations of CO₂ adsorption: **a** on Cd_{1-x}S; **b** Au_{SA}/Cd_{1-x}S; **d** CdS_{1-x}; **e** Au_{SA}/CdS_{1-x}. PDOS of CO₂ and adsorption site: **c** in Au_{SA}/Cd_{1-x}S; **f** Au_{SA}/CdS_{1-x}.

above results indicate that when CO adsorbs on Cd vacancy, it will combine with H* to further convert into HCO* and H₃CO*, which is in accordance with the observations in DRIFTS spectra of the CO₂ adsorption process.

Furthermore, according to the partial density of states (PDOS) (cf. Fig. 5f), it is observed that the interaction between CO₂ and single Au atoms in the Au_{SA}/CdS_{1-x} is weak. Different from it, there is a strong interaction between CO₂ and Cd vacancies in the Au_{SA}/Cd_{1-x}S (cf. Fig. 5c). More importantly, the C and O atoms of CO₂ molecule are bonded with two S atoms of the surface to form the S-C and S-O bonds (cf. Fig. 5b). As a result, the electrons transfer from the surface to the bonded CO₂ molecule (0.52 e) to promote its activation, resulting in C-O-C bond angle bending and elongation of both C-O bonds. To further prove the effect of different adsorption sites in the CO₂ adsorption behavior, isotope labeling is carried out on Au_{SA}/Cd_{1-x}S and Au_{SA}/CdS_{1-x} using ¹³CO₂ instead of ¹²CO₂ for the DRIFTS analysis (cf. Fig. 4b and Supplementary Fig. 16d). It is observed that, compared with using ¹²CO₂ as reactants, similar absorption bands are detected on both Au_{SA}/Cd_{1-x}S and Au_{SA}/CdS_{1-x} under ¹³CO₂ atmosphere. Meanwhile, the positions of all the absorption bands have a ¹³C frequency shift toward low wavenumber in varying degrees (2–16 cm⁻¹). In the process of ¹²CO₂ adsorption (cf. Fig. 4c), there is an absorption band detected at 1280 cm⁻¹ on both Au_{SA}/Cd_{1-x}S and Au_{SA}/CdS_{1-x}, which is assigned to the vibration of C-O bonds in CO₂⁻ (adsorption state of CO₂). In the process of ¹³CO₂ adsorption, there is a small ¹³C frequency shift (6 cm⁻¹) occurring on the surface of Au_{SA}/CdS_{1-x}. It should be noted that there is a large ¹³C frequency shift (16 cm⁻¹) of this absorption

band detected on the surface of Au_{SA}/Cd_{1-x}S. It is indicated that, compared with Au_{SA}/CdS_{1-x} surface, the adsorbed CO₂ obtains more electrons from Au_{SA}/Cd_{1-x}S surface to weaken the C-O bond, leading to a larger ¹³C frequency shift. Meanwhile, according to the value of ¹³C frequency shift, more than one C-O bonds might be bonded to the surface^{11,52}. Based on the above discussions, it is speculated that CO₂ molecule is physically adsorbed on single atoms of Au_{SA}/CdS_{1-x} surface. The formation of bonds and effective electron transfer between surface and CO₂ indicate that CO₂ molecule is chemically adsorbed on Cd vacancies of Au_{SA}/Cd_{1-x}S surface. In brief, when the type of vacancies changes from S vacancies to Cd vacancies, the CO₂ adsorption sites change from single Au atoms to the vacancies. Benefiting from this, CO₂ could be chemically bonded on the Cd vacancies instead of physical adsorption on single Au atoms. The strong interaction between CO₂ and adsorption sites (Cd vacancies) profits the formation of stable electron-transfer channels. As a result, CO₂ could obtain more electrons from the adsorption sites to promote its deep transformation.

To identify the internal factors affecting adsorption sites, the charge population of Cd_{1-x}S and CdS_{1-x} surfaces after anchoring Au nanostructures is explored by DFT calculations (cf. Fig. 6a and 6b). For the Au anchored on Cd vacancies, the electrons (0.23 e) will transfer from single Au atoms to Cd_{1-x}S to enhance the surface electron density. More importantly, the majority of electrons are localized at the neighboring Cd vacancy site. On the contrary, the direction of electron transfer between Au and CdS_{1-x} is reversed, resulting in the localization of electrons at single Au atoms (0.40 e). To further identify the electron transfer between Au and Cd_{1-x}S or CdS_{1-x}, X-ray photoelectron

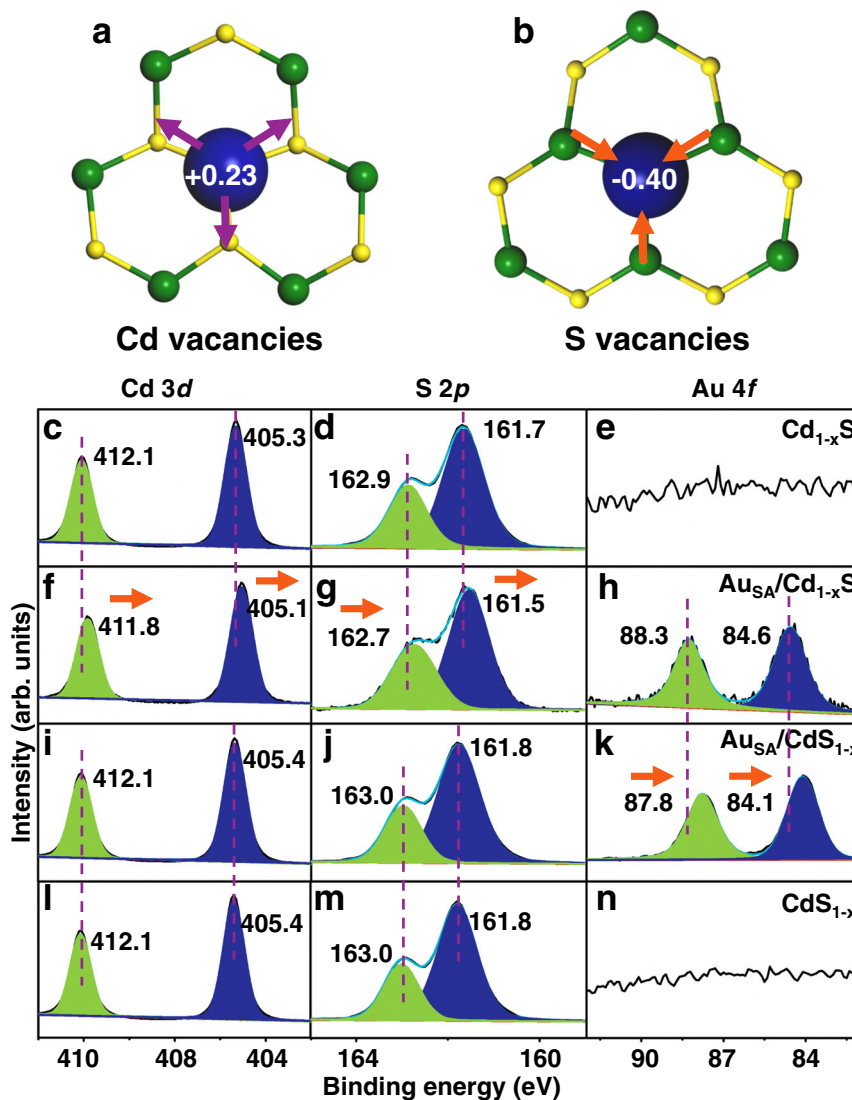


Fig. 6 Charge transfer on different surfaces. Electron transfer between Au and CdS with different types of vacancies: **a** Cd vacancies; **b** S vacancies. XPS spectra: **c–e** Cd_{1-x}S; **f–h** Au_{SA}/Cd_{1-x}S; **i–k** CdS_{1-x}; **l–n** Au_{SA}/CdS_{1-x} samples.

spectroscopy (XPS) spectra are presented in Fig. 6. For Cd_{1-x}S system (cf. Fig. 6c–h), the peaks indexed to the Cd–S bond in Cd 3d and S 2p spectra have a shift toward low binding energy (0.2–0.3 eV) compared with the pristine Cd_{1-x}S, indicating that Cd_{1-x}S receives electrons from the single Au atoms. While for CdS_{1-x} system (cf. Fig. 6i–n), the peaks corresponding to the Cd–S bond barely change after anchoring single Au atoms. It should be noted that the peaks in Au 4f spectra of Au_{SA}/CdS_{1-x} system are located at 87.8 and 84.1 eV and the binding energies are much lower (c.a. 0.5 eV) than that of Au_{SA}/Cd_{1-x}S. This suggests that the electrons are localized at single Au atoms instead of CdS_{1-x} in Au_{SA}/CdS_{1-x} system. To identify the internal factors affecting the direction of electron transfer between single Au atoms and Cd_{1-x}S or CdS_{1-x}, the potential energy plots are given in Supplementary Fig. 22. In the case of Au_{SA}/CdS_{1-x}, the potential energy of CdS_{1-x} is much lower than that of single Au atoms. Benefiting from it, there is a driving force promoting electron transfer from CdS_{1-x} to single Au atoms. Opposite to that, the potential energy of single Au atoms is lower than that of Cd_{1-x}S, resulting in the reversal of electron transfer direction. Hence, it is observed that the electrons are localized at the single Au atoms when they anchor on S vacancies. After single Au atoms anchored on Cd vacancies, the electrons will conversely

transfer from single Au atoms to Cd_{1-x}S and accumulate on Cd vacancies.

Photo-induced carrier transfer during photocatalysis. According to the DFT and XPS spectra (cf. Supplementary Fig. 23–25), it is found that with the increased content of Au, the electron transfer is gradually weakened for both Cd_{1-x}S and CdS_{1-x} systems. Hence, to further identify the underlying roles of Au content on the surface electron density, the Au/Cd_{1-x}S system is selected as the representative in the following discussion. In general, electron transfer might be related to the local electronic structure. According to PDOS in Supplementary Fig. 26, compared with the Au_{NC}/Cd_{1-x}S, the hybridization between Au 5d and S 2p orbitals in Au–S bonds is much stronger for Au_{SA}/Cd_{1-x}S. As a result, more electrons are transferring from Au 5d orbitals in single Au atoms to Cd_{1-x}S compared with Au clusters (cf. Supplementary Fig. 27). This is identified by XPS analysis in Supplementary Fig. 25. The peaks indexed to the Cd–S bond in Cd 3d and S 2p spectra for Au_{SA}/Cd_{1-x}S have a shift toward low binding energy (0.2–0.3 eV) and the Au 4f spectrum shifts to high binding energy (0.4–0.6 eV) compared with Au_{NC}/Cd_{1-x}S. It is indicated that the interaction between single Au atoms and Cd vacancies is much stronger than that with Au

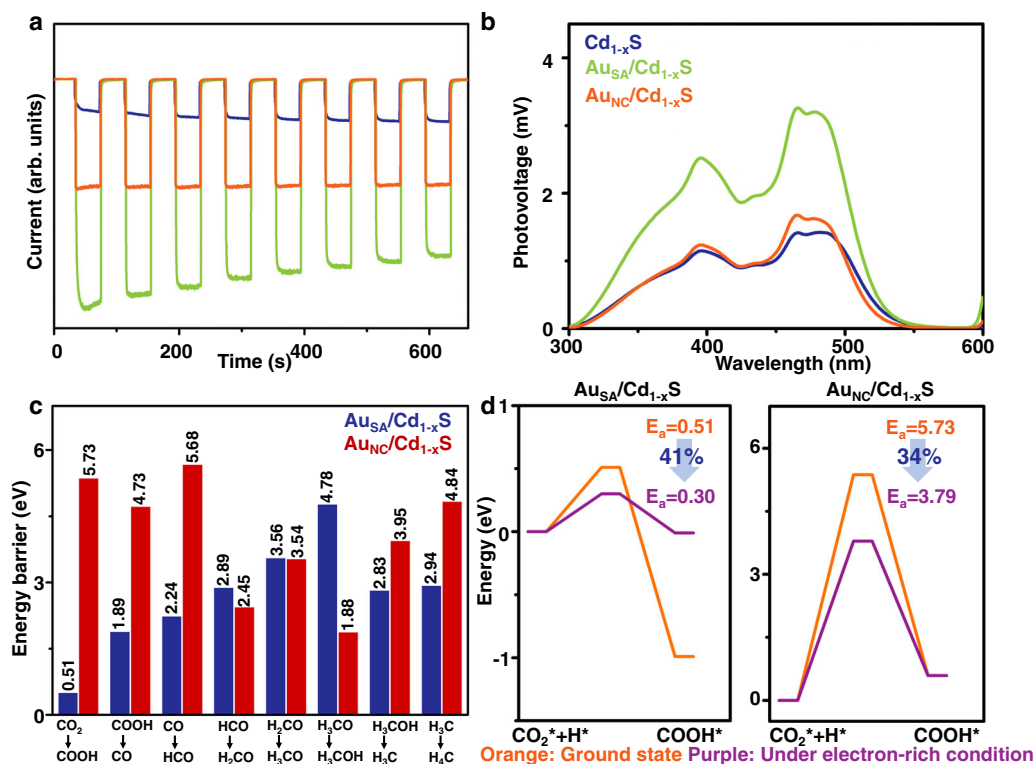


Fig. 7 Photo-induced carrier transfer and energy barriers in the process of CO₂RR based on DFT calculations. **a** Transient photocurrent response and **b** SPV spectra of Cd_{1-x}S, Au_{SA}/Cd_{1-x}S, and Au_{NC}/Cd_{1-x}S samples. **c** Energy barriers of CO₂ reduction on Au_{SA}/Cd_{1-x}S and Au_{NC}/Cd_{1-x}S. **d** Reaction profiles of CO₂ transition into COOH on Au_{SA}/Cd_{1-x}S and Au_{NC}/Cd_{1-x}S.

clusters. Benefiting from it, under light illumination, it is observed that the lifetimes of photogenerated electrons in Cd_{1-x}S are decreased from 2.95 to 0.44 ns (Au_{SA}/Cd_{1-x}S) and 2.22 (Au_{NC}/Cd_{1-x}S) (cf. Supplementary Fig. 28). It could be concluded that, compared with Au nanoclusters, the stronger interaction between single Au atoms and Cd vacancies significantly accelerates electron transfer to the surface to enhance the surface electron density under light illumination. Meanwhile, the intensity of transient photocurrent response is significantly increased with the introduction of Au (cf. Fig. 7a). Au_{SA}/Cd_{1-x}S sample reveals the highest intensity compared with Au_{NC}/Cd_{1-x}S and Cd_{1-x}S. It is suggested that single Au atoms offer a significantly higher enhancement in the surface electron density of Cd_{1-x}S compared with Au clusters. This is further identified by the surface photovoltage (SPV) in Fig. 7b. It should be noted that two peaks are appearing in the SPV spectra of Cd_{1-x}S. The peak at c.a. 400 nm corresponds to the electrons transferring from the top of valence band to the bottom of conduction band. The other one at c.a. 500 nm is assigned to the defect level introduced by Cd vacancy on the surface which is observed in the band structure (cf. Supplementary Fig. 29). Interestingly, intensities of the two peaks increase after anchoring Au nanostructures, especially the single Au atoms. It is suggested that compared with Au nanoclusters, the introduction of single Au atoms significantly promotes the enhancement of electron density on the Cd_{1-x}S surface as well as the Cd vacancies under light illumination. Meanwhile, a similar trend is observed in transient photocurrent response and SPV spectra of Au/CdS_{1-x} system (cf. Supplementary Fig. 30).

As presented in Fig. 7c and Supplementary Fig. 31, the processes of CO₂ reduction on Au_{SA}/Cd_{1-x}S and Au_{NC}/Cd_{1-x}S are further simulated by DFT calculations. Most of the energy barriers on Au_{SA}/Cd_{1-x}S are lower than that of Au_{NC}/Cd_{1-x}S, indicating that single Au atoms greatly facilitate CO₂ reduction compared with Au nanoclusters. More interestingly, the energy barrier of the first step

(CO₂+H→COOH) on Au_{SA}/Cd_{1-x}S is remarkably decreased by 91.1% relative to that over Au_{NC}/Cd_{1-x}S. This suggests that the accumulated electrons in Cd vacancies on Au_{SA}/Cd_{1-x}S not only promote the activation of CO₂ molecule, but also facilitate its further transformations. It is identified that there is no significant absorption band assigned to COOH* observed among in situ DRIFTS test over Au_{SA}/Cd_{1-x}S. Furthermore, extra electron is introduced to create an electron-rich condition in the process of CO₂ transition into COOH in Fig. 7d⁵³. Interestingly, the energy barrier on Au_{SA}/Cd_{1-x}S presents a larger decrease (41%) compared with that on Au_{NC}/Cd_{1-x}S (34%). It is suggested that, compared with Au_{NC}/Cd_{1-x}S, the enhancement of surface electron density much more facilitates the occurrence of CO₂ reduction catalyzed by Au_{SA}/Cd_{1-x}S.

In summary, we have designed and fabricated a series of Au/CdS photocatalysts. On the one hand, the types of vacancies highly affect the direction of electron transfer. That is the electrons will transfer from CdS_{1-x} to Au in CdS_{1-x} system. Quite different from it, the direction of electron transfer has been reversed in Cd_{1-x}S system, resulting in the accumulation of electrons in Cd vacancies. Hence, the adsorption of CO₂ is enabled in vacancy sites instead of Au sites. More importantly, there is a stable electron-donation channel forming between CO₂ and Cd vacancies, accelerating the transfer of accumulated electrons to CO₂ for its effective activation. On the other hand, under light illumination, when Au nanostructures change from Au nanoclusters to single Au atoms, the surface electron density is significantly increased and promotes much more electrons accumulating on the surface as well as the Cd vacancies, which is beneficial for the subsequent reaction. As a result, the CO and CH₄ generation rates of Au_{SA}/Cd_{1-x}S manifest a remarkable 160-fold and 113-fold enhancement compared with Cd_{1-x}S as well as the H₂ generation rate is promoted from 0 to 7.9 μmol g⁻¹ h⁻¹.

Methods

Synthesis of Cd_{1-x}S, CdS_{1-x} and CdS. The Cd_{1-x}S and CdS_{1-x} were synthesized via a modified hydrothermal method⁵⁴. For Cd_{1-x}S, the synthesis process as follows: first, CdCl₂·5H₂O (4 mM) was dissolved in 20 mL aqueous solution (pH = 1, marked as solution A). Meanwhile, another 20 mL aqueous Na₂S·9H₂O (8 mM) solution was prepared, marked as solution B. Then, solution B was added dropwise into solution A under continuous stirring. The mixed solution was transferred into a Teflon-lined stainless steel autoclave (inner volume: 50 mL) and held at 140 °C for 18 h in an oven. After cooling to room temperature naturally, the product was centrifuged and washed with water and ethyl alcohol several times. Finally, the obtained product was dried overnight at 60 °C under vacuum condition. The synthesis process of CdS_{1-x} and CdS were the same as that of Cd_{1-x}S except that 1 and 4 mM of Na₂S·9H₂O were added in solution B.

Synthesis of Au/Cd_{1-x}S and Au/CdS_{1-x}. The Au/Cd_{1-x}S and Au/CdS_{1-x} were synthesized by the impregnation method. For 1%Au/Cd_{1-x}S, 100 mg of Cd_{1-x}S was dispersed in 30 mL water and adding 0.2 mL HAuCl₄ solution (5 mg/mL). Then, the mixed solution was stirred at 70 °C for 6 h. The product was centrifuged and washed with water and ethyl alcohol several times and dried overnight at 60 °C under vacuum condition. The synthesis procedure of 2%Au/Cd_{1-x}S was the same as that of 1%Au/Cd_{1-x}S, except that 0.4 mL of HAuCl₄ solution was used in the experiment. Meanwhile, Au/CdS_{1-x} samples were synthesized by the same method using CdS_{1-x} instead of Cd_{1-x}S.

Photocatalytic performance measurement. Photocatalytic CO₂ reduction performance test was carried out in a closed gas system (volume: 276 mL) at atmospheric pressure and ambient temperature. First, 30 mg of photocatalyst was dispersed with H₂O in a petri dish (ø = 6 cm) and dried at 70 °C under vacuum condition. Then, petri dish was put on a stainless steel breaker with 1 mL of deionized water in the reactor, which was filled with the CO₂ (concentration: 1000 ppm; carrier gas: Ar). A 300 W Xe lamp was used as the UV-vis light source (intensity: 600 mW/cm²). Every 2 h, 1 mL of gas was taken from the reactor for qualitative analysis by gas chromatography (GC7900, Tianmei Analytical Instrument Co., Ltd., China). CO and CH₄ were detected by a flame ionization detector (FID) and a thermal conductivity detector (TCD) was used for detecting H₂. The isotope test was carried out by using ¹³CO₂ as the carbon source with the same reaction set as mentioned above and the gas products were analyzed by mass spectrometry (OmniStar™, Pfeiffer Vacuum, Germany).

In situ DRIFTS investigation. In situ DRIFTS measurements were performed on a TENSOR II FT-IR spectrometer (Bruker, Germany). The spectrometer was equipped with an in situ diffuse reflectance cell (Harrick) and a high-temperature reaction chamber (HVC). A mixture of ¹²CO₂ (20% CO₂/Ar) and H₂O vapors (humidity: 5% Rh) with a flow rate of 17 mL min⁻¹ was introduced into the Harrick cell. In case of Au_{S_A}/Cd_{1-x}S and Au_{S_A}/CdS_{1-x} samples, ¹³CO₂ (20% ¹³CO₂/Ar) was used instead of ¹²CO₂ to perform the isotope test. For CO probe test, a mixture of CO (10% CO/Ar) and H₂O vapors (humidity: 5%Rh) with a flow rate of 17 mL min⁻¹ was introduced into the Harrick cell. Before the measurement, the samples were pretreated at 100 °C for 10 min under Ar atmosphere.

Data availability

The data that support the findings of this study are available from the corresponding author upon reasonable request.

Code availability

The code to reproduce the results is available from the corresponding author upon reasonable request.

Received: 19 October 2020; Accepted: 19 February 2021;

Published online: 15 March 2021

References

- Yi, Q., Li, W., Feng, J. & Xie, K. Carbon cycle in advanced coal chemical engineering. *Chem. Soc. Rev.* **44**, 5409–5445 (2015).
- Shi, R. et al. Efficient wettability-controlled electroreduction of CO₂ to CO at Au/C interfaces. *Nat. Commun.* **11**, 3028 (2020).
- Zhao, Y. et al. Two-dimensional-related catalytic materials for solar-driven conversion of CO_x into valuable chemical feedstocks. *Chem. Soc. Rev.* **48**, 1972–2010 (2019).
- Li, Y. et al. Selective light absorber-assisted single nickel atom catalysts for ambient sunlight-driven CO₂ methanation. *Nat. Commun.* **10**, 2359 (2019).
- Hao, L. et al. Surface-halogenation-induced atomic-site activation and local charge separation for superb CO₂ photoreduction. *Adv. Mater.* **31**, 1900546 (2019).
- Chen, F. et al. Macroscopic spontaneous polarization and surface oxygen vacancies collaboratively boosting CO₂ photoreduction on BiOIO₃ single crystals. *Adv. Mater.* **32**, 1908350 (2020).
- Hu, C., et al. Coupling piezocatalysis and photocatalysis in Bi₄NbO₈X (X = Cl, Br) polar single crystals. *Adv. Funct. Mater.* **30**, 1908168 (2019).
- Li, X. et al. Selective visible-light-driven photocatalytic CO₂ reduction to CH₄ mediated by atomically thin CuIn₂S₃ layers. *Nat. Energy* **4**, 690–699 (2019).
- Kim, W., Seok, T. & Choi, W. Nafion layer-enhanced photosynthetic conversion of CO₂ into hydrocarbons on TiO₂ nanoparticles. *Energ. Environ. Sci.* **5**, 6066–6070 (2012).
- Varghese, O. K., Paulose, M., LaTempa, T. J. & Grimes, C. A. High-rate solar photocatalytic conversion of CO₂ and water vapor to hydrocarbon fuels. *Nano Lett.* **9**, 731–737 (2009).
- Cao, Y. et al. B-O bonds in ultrathin boron nitride nanosheets to promote photocatalytic carbon dioxide conversion. *ACS Appl. Mater. Inter.* **12**, 9935–9943 (2020).
- Van Deelen, T. W., Hernández Mejía, C. & de Jong, K. P. Control of metal-support interactions in heterogeneous catalysts to enhance activity and selectivity. *Nat. Catal.* **2**, 955–970 (2019).
- Liam, H. F. & Andersson, G. G. Metal clusters on semiconductor surfaces and application in catalysis with a focus on Au and Ru. *Adv. Mater.* **32**, 1904122 (2020).
- Fang, S. et al. Uncovering near-free platinum single-atom dynamics during electrochemical hydrogen evolution reaction. *Nat. Commun.* **11**, 1029 (2020).
- O'Connor, N. J., Jonayat, A. S. M., Janik, M. J. & Senthil, T. P. Interaction trends between single metal atoms and oxide supports identified with density functional theory and statistical learning. *Nat. Catal.* **1**, 531–539 (2018).
- Yan, Q. et al. Reversing the charge transfer between platinum and sulfur-doped carbon support for electrocatalytic hydrogen evolution. *Nat. Commun.* **10**, 4977 (2019).
- Zhu, W. et al. Taming interfacial electronic properties of platinum nanoparticles on vacancy-abundant boron nitride nanosheets for enhanced catalysis. *Nat. Commun.* **8**, 15291 (2017).
- Ghuman, K. K. et al. Photoexcited surface frustrated lewis pairs for heterogeneous photocatalytic CO₂ reduction. *J. Am. Chem. Soc.* **138**, 1206–1214 (2016).
- Wang, S., Guan, B. Y., Lu, Y. & Lou, X. W. D. Formation of hierarchical In₂S₃-CdIn₂S₄ heterostructured nanotubes for efficient and stable visible light CO₂ reduction. *J. Am. Chem. Soc.* **139**, 17305–17308 (2017).
- Cheng, L., Xiang, Q., Liao, Y. & Zhang, H. CdS-based photocatalysts. *Energ. Environ. Sci.* **11**, 1362–1391 (2018).
- Zhang, K., Kim, W., Ma, M., Shi, X. & Park, J. H. Tuning the charge transfer route by p-n junction catalysts embedded with CdS nanorods for simultaneous efficient hydrogen and oxygen evolution. *J. Mater. Chem. A* **3**, 4803–4810 (2015).
- Jin, J., Yu, J., Liu, G. & Wong, P. K. Single crystal CdS nanowires with high visible-light photocatalytic H₂-production performance. *J. Mater. Chem. A* **1**, 10927–10934 (2013).
- Sankar, M. et al. Role of the support in gold-containing nanoparticles as heterogeneous catalysts. *Chem. Rev.* **120**, 3890–3938 (2020).
- Wan, J. et al. Defect effects on TiO₂ nanosheets: stabilizing single atomic site Au and promoting catalytic properties. *Adv. Mater.* **30**, 1705369 (2018).
- Ishida, T., Murayama, T., Taketoshi, A. & Haruta, M. Importance of size and contact structure of gold nanoparticles for the genesis of unique catalytic processes. *Chem. Rev.* **120**, 464–525 (2020).
- Taylor, A. L., Filipovich, G. & Lindeberg, G. K. Identification of Cd vacancies in neutron-irradiated CdS by electron paramagnetic resonance. *Solid State Commun.* **9**, 945–947 (1971).
- Cavenett, B. C. Optically detected magnetic resonance (O.D.M.R.) investigations of recombination processes in semiconductors. *Adv. Phys.* **30**, 475–538 (1981).
- Nakaoka, Y. & Nosaka, Y. Electron spin resonance study of radicals produced on irradiated CdS powder. *J. Am. Chem. Soc.* **99**, 9893–9897 (1995).
- O'Keefe, M. et al. Sub-angstrom high-resolution transmission electron microscopy at 300 keV. *Ultramicroscopy* **89**, 215–241 (2001).
- Wei, Y. et al. Fabrication of inverse opal TiO₂-supported Au@CdS core-shell nanoparticles for efficient photocatalytic CO₂ conversion. *Appl. Catal. B: Environ.* **179**, 422–432 (2015).
- Wei, Y. et al. 3D ordered macroporous TiO₂-supported Pt@CdS core-shell nanoparticles: design, synthesis and efficient photocatalytic conversion of CO₂ with water to methane. *J. Mater. Chem. A* **3**, 11074–11085 (2015).
- Cai, S., Zhang, M., Li, J., Chen, J. & Jia, H. Anchoring single-atom Ru on CdS with enhanced CO₂ capture and charge accumulation for high selectivity of

- photothermocatalytic CO₂ reduction to solar fuels. *Sol. RRL* **5**, 2000313 (2021).
33. Jiao, X. et al. Partially oxidized SnS₂ atomic layers achieving efficient visible-light-driven CO₂ reduction. *J. Am. Chem. Soc.* **139**, 18044–18051 (2017).
34. Dong, C. et al. Size-dependent activity and selectivity of carbon dioxide photocatalytic reduction over platinum nanoparticles. *Nat. Commun.* **9**, 1252 (2018).
35. Zhu, Z. et al. A hierarchical heterostructure of CdS QDs confined on 3D ZnIn₂S₄ with boosted charge transfer for photocatalytic CO₂ reduction. *Nano Res.* **14**, 81–90 (2021).
36. Zhang, P., Wang, S., Guan, B. Y. & Lou, X. W. Fabrication of CdS hierarchical multi-cavity hollow particles for efficient visible light CO₂ reduction. *Energ. Environ. Sci.* **12**, 164–168 (2019).
37. Zhou, M., Wang, S., Yang, P., Huang, C. & Wang, X. Boron carbon nitride semiconductors decorated with CdS nanoparticles for photocatalytic reduction of CO₂. *ACS Catal.* **8**, 4928–4936 (2018).
38. Zhao, G. et al. Efficient photocatalytic CO₂ reduction over Co(II) species modified CdS in aqueous solution. *Appl. Catal. B: Environ.* **226**, 252–257 (2018).
39. Baltusaitis, J., Schuttlefield, J., Zeitler, E. & Grassian, V. H. Carbon dioxide adsorption on oxide nanoparticle surfaces. *Chem. Eng. J.* **170**, 471–481 (2011).
40. Ulagappan, N. & Frei, H. Mechanistic study of CO₂ photoreduction in Ti silicalite molecular sieve by FT-IR Spectroscopy. *J. Phys. Chem. A* **104**, 7834–7839 (2000).
41. Wang, T. et al. Photoreduction of CO₂ over the well-crystallized ordered mesoporous TiO₂ with the confined space effect. *Nano Energy* **9**, 50–60 (2014).
42. Yates, J. T. & Cavanagh, R. R. Search for chemisorbed HCO: the interaction of formaldehyde, glyoxal, and atomic hydrogen+CO with Rh. *J. Catal.* **74**, 97–109 (1982).
43. Ewing, G. E., Thompson, W. E. & Pimentel, G. C. Infrared detection of the formyl radical HCO. *J. Chem. Phys.* **32**, 927–932 (1960).
44. Wu, J. & Huang, C. W. In situ DRIFTS study of photocatalytic CO₂ reduction under UV irradiation. *Front. Chem. Eng. China* **4**, 120–126 (2010).
45. Liu, Y., Chen, S., Quan, X. & Yu, H. Efficient electrochemical reduction of carbon dioxide to acetate on nitrogen-doped nanodiamond. *J. Am. Chem. Soc.* **137**, 11631–11636 (2015).
46. Wagner, A., Sahn, C. D. & Reisner, E. Towards molecular understanding of local chemical environment effects in electro- and photocatalytic CO₂ reduction. *Nat. Catal.* **3**, 775–786 (2020).
47. Smith, M. L., Kumar, N. & Spivey, J. J. CO adsorption behavior of Cu/SiO₂, Co/SiO₂, and CuCo/SiO₂ catalysts studied by in situ DRIFTS. *J. Phys. Chem. C* **116**, 7931–7939 (2012).
48. Yu, Y. et al. Promotive effect of SO₂ on the activity of a deactivated commercial selective catalytic reduction catalyst: an in situ DRIFT study. *Ind. Eng. Chem. Res.* **53**, 16229–16234 (2014).
49. Xu, W., He, H. & Yu, Y. Deactivation of a Ce/TiO₂ catalyst by SO₂ in the selective catalytic reduction of NO by NH₃. *J. Phys. Chem. C* **113**, 4426–4432 (2009).
50. Wu, Q., Gao, H. & He, H. Conformational analysis of sulfate species on Ag/Al₂O₃ by means of theoretical and experimental vibration spectra. *J. Phys. Chem. B* **110**, 8320–8324 (2006).
51. Shimizu, K.-i, Higashimata, T., Tsuzuki, M. & Satsuma, A. Effect of hydrogen addition on SO₂ tolerance of silver-alumina for SCR of NO with propane. *J. Catal.* **239**, 117–124 (2006).
52. Sheng, H. et al. Carbon dioxide dimer radical anion as surface intermediate of photoinduced CO₂ reduction at aqueous Cu and CdSe nanoparticle catalysts by rapid-scan FT-IR spectroscopy. *J. Am. Chem. Soc.* **140**, 4363–4371 (2018).
53. Cao, Y. et al. Dual functions of O-atoms in the g-C₃N₄/BO_{0.2}N_{0.8} interface: oriented charge flow in-plane and separation within the interface to collectively promote photocatalytic molecular oxygen activation. *ACS Appl. Mater. Inter.* **12**, 34432–34440 (2020).
54. Guo, L. et al. Promoting charge carriers transfer of Co-S bonds in Co/CdS for enhanced photocatalytic CO₂ reduction. *Chin. Sci. Bull.* **65**, 522–532 (2019).

Acknowledgements

We gratefully acknowledge financial support from the National Natural Science Foundation of China (U1862111), Sichuan Provincial International Cooperation Project (2019YFH0164), and International Collaboration Project of Chengdu City (2017-GH02-00014-HZ). Y. Z. thanks for the Cheung Kong Scholars Programme of China. We acknowledge the National Supercomputing Center in Shenzhen for calculation support. We thank the Synchrotron radiation source at KIT, Karlsruhe, and PETRA III at DESY, Hamburg for providing the beamtime at CAT-ACT and P65 beamlines, correspondently. We also thank Dr. Anna Zimina (KIT) and Dr. Edmund Welter (DESY) for help during measurements.

Author contributions

Y.Z. conceived the research and designed the experiments. Y.Z. and M.D. designed the synthesis. Y.C. and L.G. performed the synthesis, characterization, and photocatalysis. Y.C. performed the DFT calculations. D.E.D. performed the XAS in terms of XANES and EXAFS test. C.H. performed the SPV tests. Y.L. and J.M. performed the TEM and EDS mapping with support from K.Z. Y.C. and Z.R. performed in situ DRIFTS test with support from Z.H. P.C. performed the EPR tests with support from F.D. Y.C. wrote the manuscript with support from Y.Z. All authors analyzed the data and commented on the manuscript.

Competing interests

The authors declare no competing interests.

Additional information

Supplementary information The online version contains supplementary material available at <https://doi.org/10.1038/s41467-021-21925-7>.

Correspondence and requests for materials should be addressed to Y.Z.

Peer review information *Nature Communications* thanks Pavel Afanasiev, Ekaterina Kozlova, and other, anonymous, reviewer(s) for their contributions to the peer review of this work.

Reprints and permission information is available at <http://www.nature.com/reprints>

Publisher's note Springer Nature remains neutral with regard to jurisdictional claims in published maps and institutional affiliations.



Open Access This article is licensed under a Creative Commons Attribution 4.0 International License, which permits use, sharing, adaptation, distribution and reproduction in any medium or format, as long as you give appropriate credit to the original author(s) and the source, provide a link to the Creative Commons license, and indicate if changes were made. The images or other third party material in this article are included in the article's Creative Commons license, unless indicated otherwise in a credit line to the material. If material is not included in the article's Creative Commons license and your intended use is not permitted by statutory regulation or exceeds the permitted use, you will need to obtain permission directly from the copyright holder. To view a copy of this license, visit <http://creativecommons.org/licenses/by/4.0/>.

© The Author(s) 2021